Effect of Moderate Electropulsing on Nb Multiterminal Transport Bridges

S. Marinković,[1,†] E. A. Abbey,[1,2,†] D. A. D. Chaves,[2,3] S. Collienne,[1] E. Fourneau,[1,4] L. Jiang,[1,5] C. Xue,[6] Y. H. Zhou,[5,7] W. A. Ortiz,[2] M. Motta,[2] N. D. Nguyen,[4] A. Volodin,[3] J. Van de Vondel,[3] and A. V. Silhanek[1,*]

[1] *Experimental Physics of Nanostructured Materials, Q-MAT, CESAM, Université de Liège, Sart Tilman B-4000, Belgium*

[2] *Departamento de Física, Universidade Federal de São Carlos, São Carlos, SP 13565-905, Brazil*

[3] *Quantum Solid-State Physics, Department of Physics and Astronomy, KU Leuven, Celestijnenlaan 200D, Leuven B-3001, Belgium*

[4] *Solid-State Physics—Interfaces and Nanostructures, Q-MAT, CESAM, Université de Liège, Sart Tilman B-4000, Belgium*

[5] *School of Aeronautics, Northwestern Polytechnical University, Xi'an 710072, China*

[6] *School of Mechanics, Civil Engineering and Architecture, Northwestern Polytechnical University, Xi'an 710072, People's Republic of China*

[7] *Key Laboratory of Mechanics on Disaster and Environment in Western China, Ministry of Education of China, Department of Mechanics and Engineering Sciences, Lanzhou University, Lanzhou 730000, China*

(Received 18 November 2022; revised 13 February 2023; accepted 29 March 2023; published 3 May 2023)

We investigate targeted and localized material modifications produced by electropulsing of Al-capped Nb microbridges with a multiterminal configuration. The affected regions of the Nb/Al bilayer terminals are revealed by an in-lens secondary-electron detector in a scanning electron microscope and by Kelvin-probe force microscopy, both suggesting a decrease in the work function in the modified areas. In contrast, the affected areas are neither apparent through an Everhart-Thornley secondary-electron detector nor through atomic force microscopy, which indicates little morphological change in the microstructure. In addition, we demonstrate that the extent of the electroannealed regions is strongly influenced by the terminal geometry. These results are captured by complementary finite-element modeling, which permits us to estimate that a threshold temperature of 435 ± 35 K is needed to induce material modifications. These findings provide further insights into the subtle modifications produced by gentle electroannealing of Nb/Al microstructures and represent a step forward towards mastering this emerging nanofabrication technique.

DOI: 10.1103/PhysRevApplied.19.054009

I. INTRODUCTION

Niobium is a material of choice for a variety of superconducting applications, including radio-frequency (rf) accelerator cavities [1–3], quantum interference devices [4–6], Josephson tunnel junctions and weak links [7,8], superconducting resonators and filters [9–11], quantum bits [12–14], and flexible superconducting transmission lines [15,16]. The reasons for this privileged position are manifold: niobium is the element with the highest superconducting critical temperature, it develops stable oxide coatings (NbO, NbO_2, and Nb_2O_5) that protect the superconducting phase, it exhibits long-term stability under repeated thermal cycling, it can be nanostructured by additive or subtractive lithography, it is malleable and ductile, and it has low toxicity.

More importantly, the possibility of performing surface treatments such as thermal etching, electropolishing, annealing in a controlled atmosphere, and buffered chemical polishing allows further optimization of the properties of Nb, such as achieving a low microwave surface resistance desired for boosting the efficiency of rf cavities [17]. Naturally, these procedures are applied homogeneously to the entire sample or device, and do not allow spatial selectivity. An elegant approach to overcoming this limitation has recently been proposed, based on local annealing of the sample by the combined effects of Joule heating and electromigration [18]. This technique has been successfully implemented to tune the properties of Nb-based superconducting weak links [19], superconducting

*asilhanek@uliege.be

†S.M. and E.A.A. contributed equally to this work.

quantum interference devices [20], multiterminal junctions [21], and for the fabrication of nanoheaters [22]. In the applications listed above, a substantial resistance increase was achieved by severe electromigration, and the resulting structural modifications and possible alloying were amply illustrated and discussed. In contrast, the consequences of electromigration of Nb limited to an increase in resistance of a few percent have remained largely unexplored so far.

In this paper, we acquire valuable insights on the subtle changes of the material induced by electropulsing of Nb/Al systems. We focus particularly on the low-stress regime, corresponding to currents slightly above the onset of electroannealing and giving rise to an increase in resistance of a few percent. A subtle induced change is a reduction of the work function in the targeted region, likely associated with local oxidation triggered by thermal effects, although no microstructural modifications are revealed. By comparing the spread and shape of the affected area with thermal maps computed through finite-element modeling, we are able to conclude that temperatures above 435 K are needed to induce sizable modifications in the material. Several funnel-shaped constrictions with different angles are fabricated to demonstrate the possibility of controlling the extent of the affected area via its geometry. Identification of the key parameters that permit one to master the local modifications of Nb constrictions and understanding which material properties are affected by electropulsing represent relevant steps needed to achieve *in situ* superconducting weak links and normal leads.

II. EXPERIMENTAL DETAILS

Resist patterns consisting of a double PMMA/co-PMMA layer are prepared by electron-beam lithography on a Si/SiO_2 substrate (750 ± 50 μm Si, 300 ± 25 nm SiO_2) using a Pioneer 2 nanofabrication system from Raith GmbH. Subsequently, a Nb thin film (approximately 50 nm thick) is deposited using radio-frequency magnetron sputtering in a chamber previously pumped down to 10^{-8} mbar at a deposition rate of 1 Å/s in an Ar pressure of 5.3 mbar. Without breaking the vacuum, the sample is then capped with a 7-nm-thick Al layer by electron-beam evaporation. The thickness of the Al capping layer is chosen to be slightly greater than that of the native oxide layer of Al [23], so that it acts as a protective layer for the Nb [24]. If left uncapped, the Nb would naturally develop a coating oxide layer, with similar protective effects to those of the native oxide layer on Al. The final structure is revealed after a conventional liftoff process in warm (approximately 50 °C) acetone.

Figure 1 shows the sample layout, in which a 2-μm-wide central transport bridge is connected to ten terminals, symmetrically placed with respect to the central axis of the bridge. All ten terminals are 1.25 ± 0.05 μm wide at the point of contact (the junction) with the bridge. In order to investigate the possible influence of the junction geometry on the properties of the zone affected by electropulsing, the upper row of junctions, labeled from 1 to 5, form different angles ($\theta = 90°$ to 50°, respectively, in steps of $-10°$) with the central axis of the bridge. We consider the complement of this angle to be the funnel angle, $90° - \theta$. The junctions in the lower row are intended for the sole purpose of measuring the electric potential drop and remain unaffected by the electropulsing process.

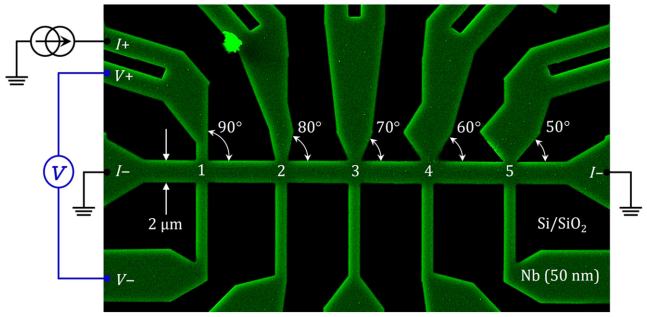

FIG. 1. False-color scanning-electron-microscopy image of one of the Nb multiterminal transport bridges. The circuitry and polarity of the current source are indicated for the case of electropulsing of junction 1.

In order to address a particular junction without affecting the neighboring junctions, the current is fed through the upper contact corresponding to that particular junction, and a current sink is connected to the left and right extremes of the transport bridge. The voltage drop across the junction is measured between the upper and the opposing lower contact. For the sake of clarity, Fig. 1 shows the polarity of the current source and voltmeter when junction 1 is modified. This strategy has been recently discussed by Collienne *et al.* for the case of strongly modified Nb trijunctions [21]. The samples are contacted by needle probes while they are excited and probed by a dual-channel source meter (Keithley 2612B). The findings reported in this paper were reproduced in five different samples.

Kelvin-probe force microscopy (KPFM) [25,26] measurements are conducted under ambient conditions in a scanning probe microscope (Agilent Technologies, model 5500). The setup is equipped with conductive platinum silicide probes from NANOSENSORS (PtSi-FM) with a tip radius of curvature around 25 nm and a nominal force constant of 2.8 N/m. Using Kelvin-probe force microscopy, an evolution of atomic force microscopy (AFM), a difference in work function between the probe tip and the sample can be measured locally. An ac voltage is applied to the cantilever of the KPFM probe, causing an oscillating electrostatic force between its tip and the sample, while the corresponding signal is measured by a lock-in amplifier. A dc voltage is then applied to

the probe tip in order to minimize the oscillations in the electric potential and the cantilever. This dc voltage represents the difference in electric potential between the tip and the sample, and hence the difference in work function.

III. ELECTROPULSING PROTOCOL AND METHODOLOGY

The electropulsing protocol consists of applying current pulses for 1 s with a linearly increasing amplitude. A similar technique has been successfully applied to other materials [27–30]. The resistance of the sample is probed during the pulses (R_{max}) and between the pulses (R_{min}). The time between two consecutive electropulses is 25 s. This experiment is performed under ambient conditions. Figure 2 shows the resulting evolution of R_{max} (red lines) and R_{min} (blue lines) as a function of the amplitude of the pulsed current for each of the five junctions. The resistance $R_{max}(I)$ initially increases quadratically as a result of Joule heating and the finite temperature coefficient of resistance. At high current amplitudes, a sudden upturn indicates the onset of irreversible changes in the sample. A more convenient parameter, able to separate the irreversible changes occurring in the sample from the reversible Joule-heating contribution, is R_{min}, obtained with a probe current of 100 μA. Indeed, pulses of small amplitude lead to no modification of R_{min}, as manifested by a nearly current-independent resistance. Beyond a certain threshold current density, a slight decrease in resistivity is systematically observed. This effect can be linked to the relief of structural stress during a mild Joule annealing process. This initial improvement in the sample is followed by a rapid increase in the resistance, likely associated with irreversible oxidation of the Nb at the addressed junction. We limit the excess resistance produced by this process to less than 10% for each junction.

Note that even though the narrowest constriction in each junction has the same width, the electropulsing curves are not identical for different junctions. This observation suggests that the modifications produced in the junctions may not be dictated solely by the current crowding at the constriction, but that the funnel angle may play an important role as well. It is also interesting to observe that the maximum current amplitude I_{max} needed to induce the desired resistance increase varies nonmonotonically with the funnel angle and is maximized around 60°–70°. This result is reproduced for three different samples, as shown in the inset of Fig. 2. A plausible explanation for this fact could be unwanted residual Nb, which tends to round the sharp corners in the junctions and is apparent for intermediate funnel angles (see the AFM images in Appendix A). Indeed, it is expected that current crowding in sharp bends [31] will tend to reduce the threshold applied current for triggering the electromigration process.

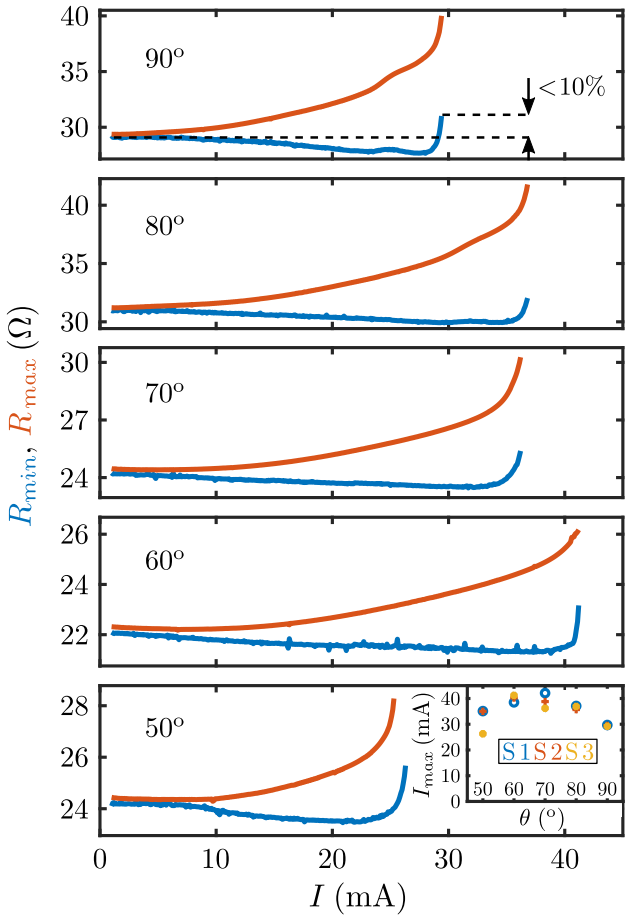

FIG. 2. Resistance probed during (R_{max}) and after (R_{min}) a current pulse of amplitude I for the five junctions shown in Fig. 1. The maximum current amplitude is set such that the initial resistance R_{min} increases by less than 10%. Electropulsing is performed under ambient conditions. The inset shows the maximum current I_{max} needed to obtain a 10% increase in resistance for three different devices labeled S1, S2, and S3.

IV. VISUALIZATION OF ELECTROPULSING-INDUCED JUNCTION MODIFICATIONS

Let us now analyze the induced modifications in each junction after the electropulsing process described above. To that end, we use several microscopic inspection techniques, including atomic force microscopy, scanning electron microscopy (SEM), and Kelvin-probe force microscopy. AFM measurements (shown in Appendix A) do not reveal any structural change after electropulsing. Consistently, no hint of modifications is observed in SEM images collected with an Everhart-Thornley (ET) detector, shown in Fig. 3(a). This detector collects mainly spatially spread type-2 secondary electrons (SE2) and should be

able to reveal nanoscale morphological changes on the sample surface. In contrast, the in-lens image shown in Fig. 3(b) evidences a clear change of contrast in the electropulsed junctions. The in-lens detector collects mainly SE1 electrons generated near the upper region of the beam-sample interaction volume and therefore provides direct information about the sample surface. These images are acquired with an accelerating voltage of 2 kV, which, according to Ref. [32], implies a penetration depth of the primary electrons into the Nb/Al bilayer of approximately 35 nm. However, the primary factor determining the emission of secondary electrons (the so-called electron yield) is essentially the surface potential (work function). Indeed, the fact that the affected regions appear brighter than the unaffected parts of the sample implies a higher electron yield, associated with a lower work function in the affected area. In order to verify this hypothesis, we carry out KPFM measurements, as shown in Fig. 3(c). In this image, red (blue) color indicates a high (low) work function. There is a close correlation between the areas with a high electron yield and those where the work function is suppressed.

A possible explanation for the observed modification of the sample surface after electropulsing is local oxidation of the Al capping layer. Indeed, it has been recently shown that secondary-electron emission is directly influenced by oxidation of an aluminum surface [33]. In particular, for oxide layers thicker than 0.4 nm, the electron emission has been shown to increase (and therefore the work function decreases). The work function of the oxide layer is also expected to be lower than that of the metallic aluminum [34]. More interestingly, in addition to oxidation, it has been shown that physisorption and chemisorption of O and C strongly influences the work function and the secondary-electron emission [35,36]. These experimental findings have recently been confirmed by first-principles studies [37]. This phenomenon may also account for the observed decrease in the work function in the Nb/Al junctions investigated.

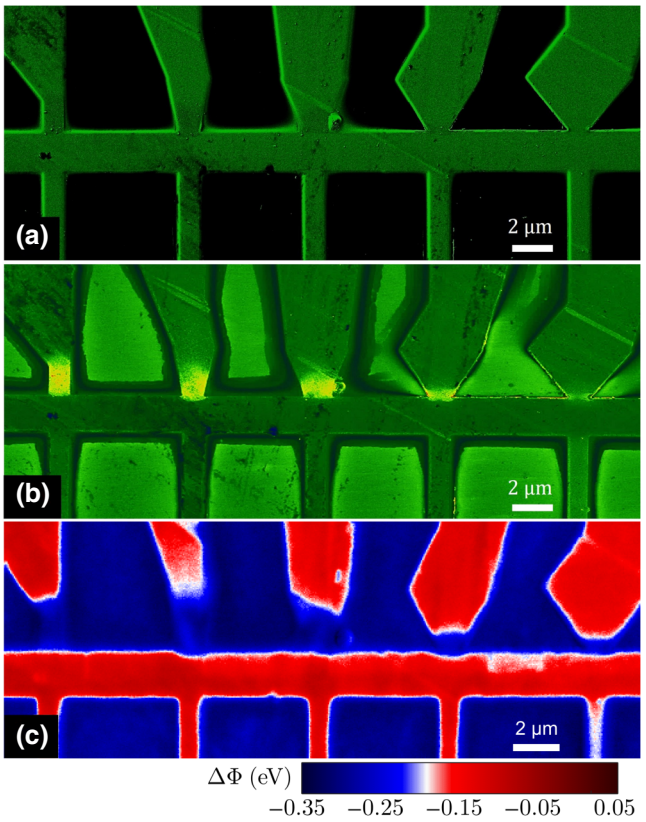

FIG. 3. Microscopic inspection of a Nb/Al device after the electropulsing procedure shown in Fig. 2. (a) SEM images obtained with an ET detector do not reveal any change that could be attributed to the electropulsing process. (b) An in-lens SEM image obtained at 2 kV demonstrates higher contrast in the junctions that have been electropulsed. (c) KPFM images of all junctions reveal a lower work function (blue) in the regions that have been electropulsed.

V. FINITE-ELEMENT MODELING

Oxygen diffusion is assisted by the local increase in temperature during the electropulsing process, and therefore estimating the temperature profile in the junctions is of paramount importance for identifying the extent of the affected area. An interesting feature observed in Fig. 3 is the fact that the affected region shrinks as the funnel angle increases. In order to understand the origin of this effect, we perform finite-element modeling taking into account the exact geometry of the samples, obtained from analysis of the SEM images. The thickness of the Nb/Al samples, $h = 62$ nm, obtained from atomic-force-microscopy (see Appendix A), is assumed uniform. Simulations assuming a pure 62-nm-thick Nb film or a Nb(55 nm)/Al(7 nm) bilayer give very similar results. This is due to the fact that most of the current flows through the Nb layer as a consequence of the high resistivity of the Al layer (300 $\mu\Omega$ cm), which can be attributed to a reduction of the mean free path due to increased diffusion effects [38]. The simulation solves the stationary heat equation

$$\nabla \cdot \mathbf{q} = Q_e, \tag{1}$$

where $\mathbf{q} = -k\nabla T$ is the heat flux density in W/m^2 and $Q_e = \rho J^2$ is the local Joule heating, $\mathbf{J} = (1/\rho)\mathbf{E}$ being the current density in A/m^2 and $\mathbf{E} = -\nabla V$ the electric field in V/m. The average thermal conductivities κ for Nb/Al and Si are assigned values of 54 [39] and 130 W/(K m) [40], respectively. The normal-state resistivity $\rho(T)$ of the sample exhibits an approximately linear temperature dependence $\rho(T) = \rho_0(1 + \alpha(T - 300))$, where $\alpha = 2.5 \times 10^{-3}$ K^{-1} is the thermal coefficient and ρ_0 is the resistivity at 300 K. The electric potential distri-

bution for the Nb layer is obtained by solving Poisson's equation

$$\nabla^2 V = 0. \tag{2}$$

The boundary condition for Eq. (1) sets the temperature at the bottom of the substrate to room temperature (see inset of Fig. 4), while three conditions are needed for Eq. (2): one for the current input and two for the current output (as an example, see Fig. 1 for junction 1). The two equations (1) and (2) are coupled by the Joule heating term Q_e. The imperfect contact between the Nb and Si imposes a thermal resistance R_{therm}, which reduces the heat removal towards the substrate:

$$q_{\text{int}} = (T_{\text{Nb}} - T_{\text{Si}})/R_{\text{therm}}, \tag{3}$$

where q_{int} is the heat flux density into the substrate, and T_{Nb} and T_{Si} are the temperatures of the sample and the substrate, respectively. R_{therm} is the effective thermal resistance in $\text{K m}^2/\text{W}$, considering the contribution of the thermal conductivity of the SiO_2 layer and the thermal resistance of the two interfaces, Nb/SiO_2 and SiO_2/Si [41,42]. As an example, when subjected to a succession of current pulses, junction 3 exhibits the resistance evolution represented by the blue curve in Fig. 4. Simulations without taking into account the thermal resistance

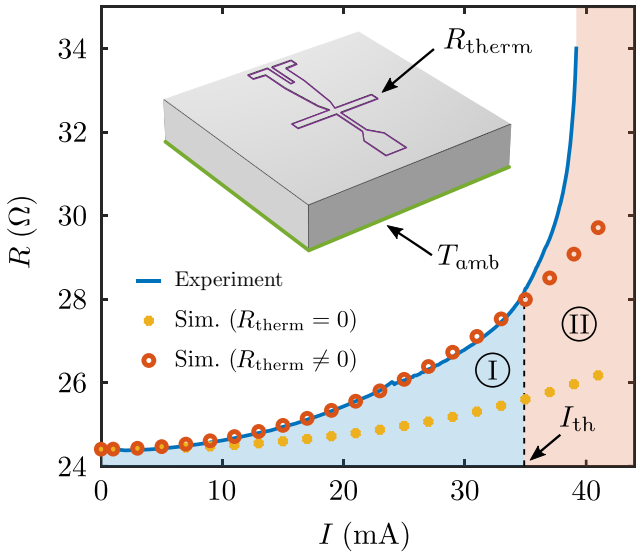

FIG. 4. Typical resistance versus current (blue curve) observed during an electropulsing experiment, together with simulations without (yellow dots) and with (red circles) thermal resistance. The blue curve corresponds to $R_{\text{max}}(I)$ in Fig. 2. The simulations highlight the existence of zones I and II, where the transition between them at the threshold current I_{th} corresponds to the appearance of irreversible alterations in the transport properties of the sample.

($R_{\text{therm}} = 0$) are shown by the yellow dots and show that the heating is insufficient to account for the experimentally observed resistance increase. The thermal resistance, $R_{\text{therm}} = 2.61 \times 10^{-8}\ \text{K m}^2/\text{W}$, is determined by iteration until the early states of electropulsing ($I < 20$ mA) are satisfactorily fitted (red circles). This value of R_{therm} is unique and is the same for all junctions. The threshold current I_{th} beyond which irreversible changes occur in the junction is defined as the current for which the modeling underestimates the experimental value of the resistance, which leads to a distinction between two zones. Zone I, for currents lower than the threshold current ($I < I_{\text{th}}$), shows a reversible parabolic profile characteristic of the Joule effect without structural modifications. Zone II ($I > I_{\text{th}}$) is characterized by a sudden increase in the resistance due to irreversible alterations of the material properties.

The electropulsing curves and simulations of five junctions in the same sample are shown in the upper row of Fig. 5. An average resistivity $\rho_0 = 37 \pm 3\ \mu\Omega\,\text{cm}$ is determined for the Nb/Al bilayer to fit the value of the resistance at low current. The middle row of Fig. 5 shows the current-density profiles for the applied current I_{th}. Independently of the total injected current, we observe that the current density becomes more inhomogeneous as the funnel angle increases, leading to maximum current crowding in junction 5. The temperature maps, given in the bottom row, are compared with the affected areas in Figs. 3(b) and 3(c) to determine the temperature T_{bound} at the boundary of the affected area in which the work function is modified. The isothermal contours are plotted as dotted lines together with the corresponding threshold temperature T_{bound}, which can be estimated as approximately 435 ± 35 K. This temperature is to be compared with the results reported in Ref. [43] concerning the growth kinetics of thin aluminum oxide films formed by dry thermal oxidation of a bare Al(431) substrate under a partial oxygen pressure of 1.33×10^{-4} Pa. The authors of that study identified a threshold temperature of 573 K below which an amorphous Al oxide film develops that attains a limiting thickness, whereas above this threshold the growth of the Al oxide layer is not impeded at a limiting thickness. In the present study, the partial oxygen pressure under atmospheric conditions is substantially higher, thus likely reducing the threshold temperature needed for steady growth of the Al oxide layer. Previous investigations via X-ray photoemission spectroscopy [44] have demonstrated that Al tends to wet the surface of Nb. This suggests that the excess Al that is not used in the formation of Al_2O_3 will diffuse easily through grain boundaries, leaving a thin uniform coverage on the Nb grains, sufficient to protect them from oxidation. In other words, part of the metallic Al lies between the Al_2O_3 and the Nb substrate, and also in the Nb grain boundaries.

In addition to the oxidation of the Al capping layer, there is a simultaneous process of Nb oxidation taking

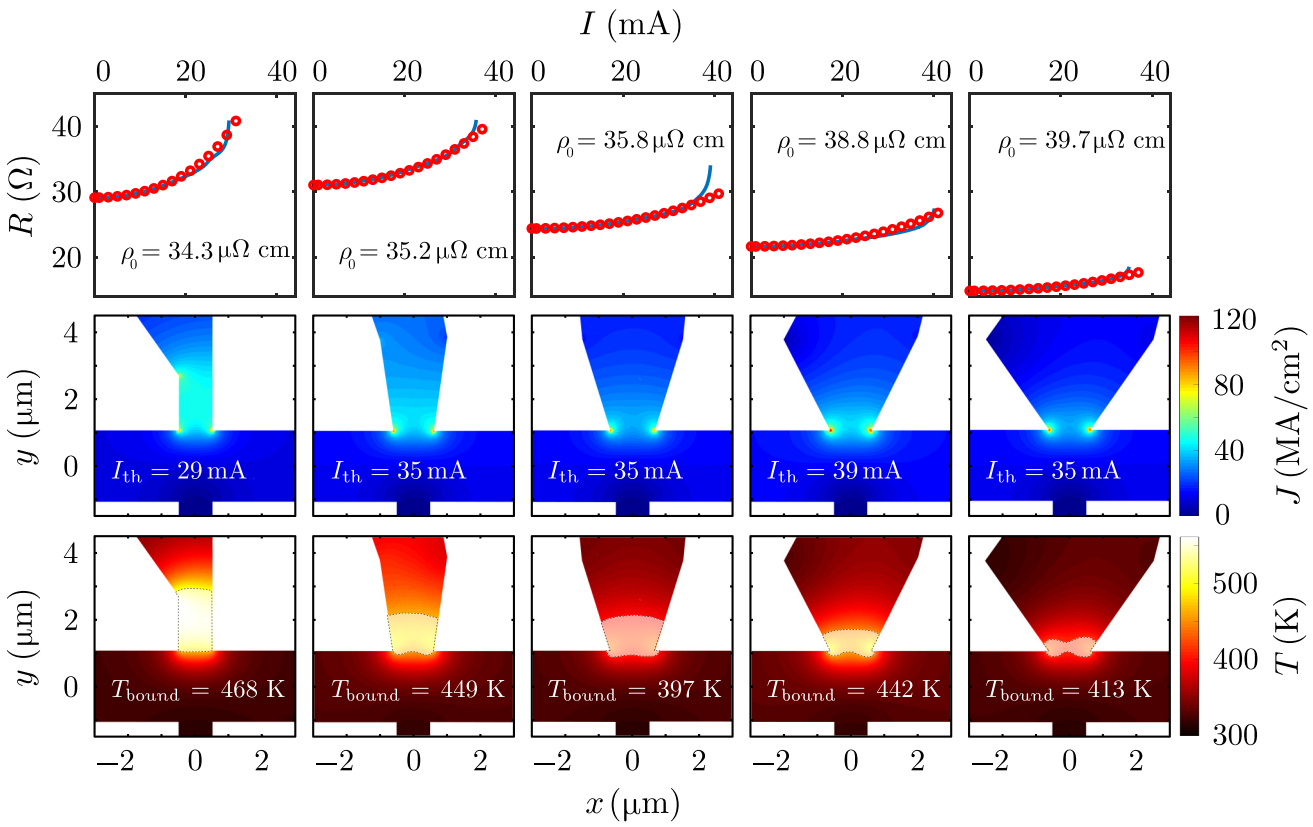

FIG. 5. Simulation results for five junctions in the same sample. The electropulsing measurements (blue curves) are shown together with simulations (red circles) in the first row. Current-density maps corresponding to the current I_{th} are shown in the second row. The images in the third row illustrate the temperature distributions, with the dashed curves denoting the isothermal curves $T = T_{\text{bound}}$ surrounding the regions in which the work function is modified.

place at the vertical walls of the Nb structure, which are not protected by the Al capping. It is known that Nb and Nb_2O_5 exhibit low diffusivity below 400 K, yielding good long-term stability, including thermal cycling up to 400 K [45]. In other words, it is not surprising that the resistivity increases in the locations where the local temperature exceeds 400 K. The numerical simulations also show a highly inhomogeneous local temperature rise, with a hot core reaching above 550 K. The fact that above 570 K the oxidation of Nb consists mainly in exponential growth of the diffusion-controlled oxygen uptake [45] suggests that the hottest part of the junction may undergo bulk modifications as well [44]. This is consistent with the development of a double-step superconducting transition after electropulsing, as shown in Appendix B. There is a possibility of some Nb-Al alloying at the interface, since a finite solubility (approximately 8 at % Al) exists in the Nb-Al phase diagram; however, in view of the rather low temperatures achieved during the electroannealing process (compared with the melting temperature $T_m > 1000\,^{\circ}\text{C}$), it is unlikely that this influences a substantial portion of the device. It is known that Nb-rich alloys (approximately 75 at % Nb) synthesized with an A-15 structure can exhibit superconducting transition temperatures well above that of bulk Nb. It is not surprising that we do not observe any hint of this phase, due in part to the commonly recognized difficulty of achieving both the necessary order and the necessary stoichiometry.

VI. CONCLUSION

In summary, we demonstrate the possibility of changing the properties of selected individual Nb junctions in a device with an arbitrary number of terminals through electropulsing. This is an appealing approach by virtue of its simplicity, which permits nanofabrication without complex overlay processing and extra deposition steps. In addition, a large degree of selectivity is observed: unaddressed junctions remain intact, and those targeted can, to some extent, be tuned by combining purposely predefined geometries and/or controlling the amplitude of the electropulsed current. As an illustration, this technique could allow us to transform a series of Nb contacts in superconductor-normal-superconductor junctions or to transform them into normal contacts. The current paper

focuses on minor modifications of the material properties (using a low current amplitude), for which no structural change is revealed. In this limit, the affected area becomes apparent through in-lens imaging in a scanning electron microscope and as contrast in Kelvin-probe force microscopy. Both of these characterization techniques point to a reduction of the work function and an enhancement of the secondary-electron yield in the affected area. This phenomenon has been investigated in the past and can be attributed to physisorption and chemisorption of O and C atoms. It is worth noting that in a recent report on electromigrated $YBa_2Cu_3O_7$ nanoconstrictions [46], the affected area becomes apparent in KPFM, suggesting the universality of this technique for tracking local modifications of material properties. Complementary finite-element modeling using the exact geometry of the samples experimentally investigated suggests that the affected area is hotter than 435 K. The current flourishing of niobium-based superconducting devices, together with continuous progress in the Nb thin films employed in transmon qubit architectures and the critical role played by oxygen vacancies as a decoherence mechanism, make the findings in this paper timely, since they reveal the severe implications of applying moderate currents in those devices.

ACKNOWLEDGMENTS

The authors acknowledge support from the EU COST action SUPERQUMAP CA21144, the Fonds de la Recherche Scientifique—FNRS under Grants No. PDR T.0204.21 and No. CDR J.0176.22, and the Research Foundation Flanders (FWO, Belgium), Grant No. G0A0619N. This work was partially supported by the São Paulo Research Foundation (FAPESP, Grant No. 2021/08781-8 and 2022/03124-1), the National Council for Scientific and Technological Development (CNPq, Grants No. 316602/2021-3 and No. 309928/2018-4), and Coordenação de Aperfeiçoamento de Pessoal de Nível Superior, Brazil (CAPES), Finance Code 001. E.A.A. and D.A.D.C. acknowledge Capes-PDSE Grants No. 88881.624496/2021-01 and No. 88881.624531/2021-01, respectively. S.M. acknowledges support from FRS-FNRS (ASP Research Fellowship). The work of L.J. was supported by the China Scholarship Council.

APPENDIX A: ATOMIC-FORCE-MICROSCOPY PROFILE

A line profile of junction 1 obtained by atomic force microscopy along the white dashed line in Fig. 6, is given by the blue curve in the inset of the bottom right panel in Fig. 6. From this measurement, we can extract a height $h_{Nb} \sim 62$ nm, which includes the 7-nm-thick Al capping layer. The red dashed line shows the profile used in the simulations, in which the width L_{Nb} is determined from the SEM image. Note that the AFM profile does not show vertical walls. This can be attributed in part to the tip-sample convolution effect [47].

Following electropulsing, AFM analysis is conducted on all junctions. It is evident from the first row of Fig. 6 that there are no significant structural modifications. The

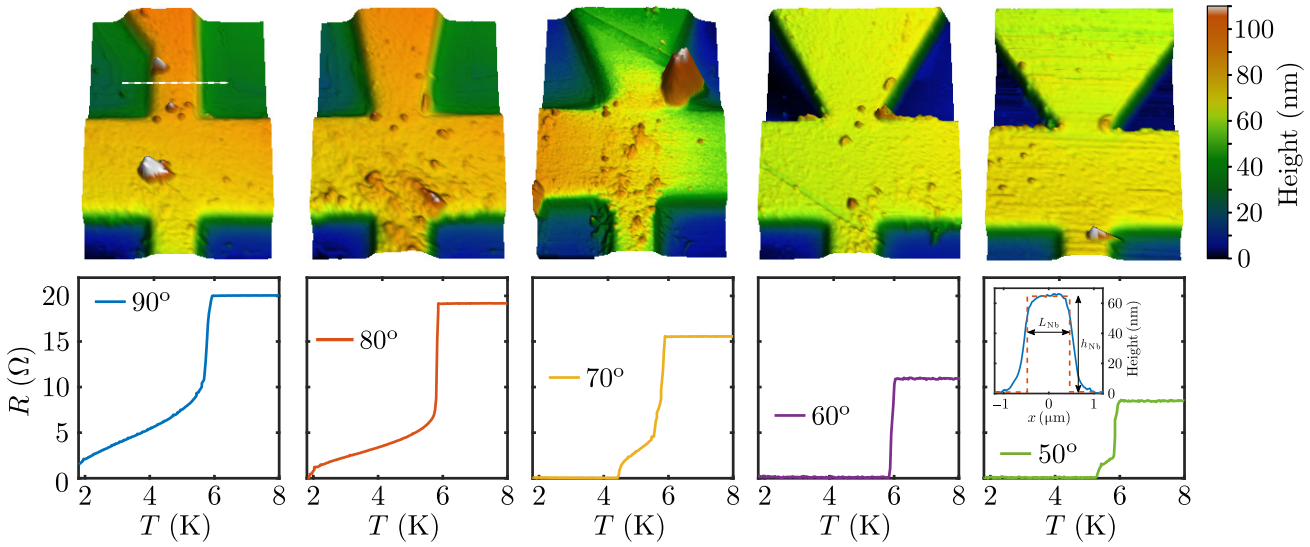

FIG. 6. After electropulsing, AFM inspection is performed on all junctions (top row). As evidenced by these images, there is no structural change following electropulsing. The bottom row shows the corresponding $R(T)$ curves for all the junctions, measured with an applied current $I = 1$ μA after a subsequent electropulsing process. The height profile of a cross section along the white dotted line in junction 1 is given by the blue curve in the inset of the bottom right panel. The red dotted lines represent the profile used in the simulations.

spikes observed in the AFM images result from residual resist traces after liftoff.

APPENDIX B: SUPERCONDUCTING TRANSITION OF EACH JUNCTION AFTER ELECTROPULSING

The resistance-versus-temperature curves obtained for the addressed junctions (labeled as indicated in Fig. 1) after electropulsing are shown in the bottom row of Fig. 6. In most cases the electropulsing leads to a two-step superconducting transition: as the temperature decreases, the first resistance drop occurs at about $T_c^0 = 5.8$ K, corresponding to a superconducting transition in the part of the Nb bridge between the voltage probes that remains unaffected by the electropulsing. This is followed by a second drop, to zero resistance, at a lower temperature, which corresponds to the area affected by the electropulsing process. Note that the extent of the affected area is larger for junction 1, which explains the larger decrease in the superconducting critical temperature. The fact that the critical temperature is substantially reduced with respect to the bulk value (9.25 K) is a consequence of the fabrication method, which includes a liftoff procedure. Since Nb is a refractory material requiring high target temperatures, significant heating and outgassing of the resist lead to a reduced critical temperature [48].

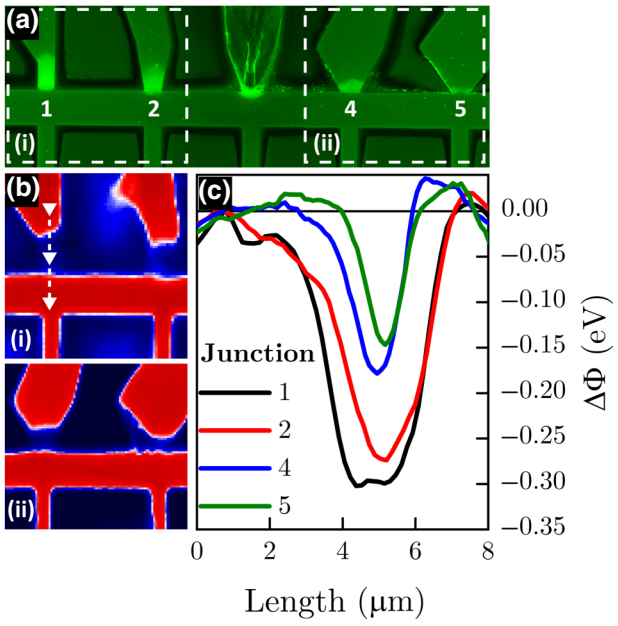

FIG. 7. (a) SEM in-lens image of device B, exhibiting higher contrast close to the electropulsed constrictions. During the experiment, the middle junction is damaged and therefore is not considered in the analysis. (b) KPFM images of junctions 1 and 2 [region highlighted by the dashed rectangle (i) in (a)] and of junctions 4 and 5 [region highlighted by the dashed rectangle (ii)]. As in the main text, red-colored regions are associated with higher values of the work function than blue-colored ones are. This is explicitly shown in the profiles in (c), where the work-function variation ($\Delta\Phi$) around each junction is plotted following the direction indicated by the white arrow across junction 1.

APPENDIX C: KELVIN-PROBE FORCE MICROSCOPY

The observations described in the main text are corroborated by KPFM measurements on similar devices, one of which is presented in Fig. 7. Although one constriction is damaged during electropulsing, a comparison between the in-lens SEM and KPFM images in Figs. 7(a) and (b) reveals a close correlation of the regions affected by the process. Furthermore, the profiles of the work-function variation ($\Delta\Phi$) displayed in Fig. 7(c) reveal unmistakably that these regions experience a drop in work function.

[1] H. Padamsee, J. Knobloch, and T. Hays, *RF Superconductivity for Accelerators* (Wiley-VCH, New York, 2008), Vol. 2.

[2] P. Bernard, D. Bloess, W. Hartung, C. Hauviller, W. Weingarten, P. Bosland, and J. Martignac, Superconducting niobium sputter-coated copper cavities at 1500 MHz, Part. Accel. **40**, 487 (1992).

[3] D. Proch, Superconducting cavities for accelerators, Rep. Prog. Phys. **61**, 431 (1998).

[4] S. K. Lam and D. L. Tilbrook, Development of a niobium nanosuperconducting quantum interference device for the detection of small spin populations, Appl. Phys. Lett. **82**, 1078 (2003).

[5] R. Kleiner, D. Koelle, F. Ludwig, and J. Clarke, Superconducting quantum interference devices: State of the art and applications, Proc. IEEE **92**, 1534 (2004).

[6] M. Mück, M. O. André, J. Clarke, J. Gail, and C. Heiden, Radio-frequency amplifier based on a niobium dc superconducting quantum interference device with microstrip input coupling, Appl. Phys. Lett. **72**, 2885 (1998).

[7] V. Bouchiat, M. Faucher, C. Thirion, W. Wernsdorfer, T. Fournier, and B. Pannetier, Josephson junctions and superconducting quantum interference devices made by local oxidation of niobium ultrathin films, Appl. Phys. Lett. **79**, 123 (2001).

[8] C. J. Muller, J. M. V. Ruitenbeek, and L. J. D. Jongh, Experimental observation of the transition from weak link to tunnel junction, Physica C **191**, 485 (1992).

[9] D. E. Oates and G. F. Dionne, Magnetically tunable superconducting resonators and filters, IEEE Trans. Appl. Supercond. **9**, 4170 (1999).

[10] S. S. Attar, S. Setoodeh, P. D. Laforge, M. Bakri-Kassem, and R. R. Mansour, Low temperature superconducting tunable bandstop resonator and filter using superconducting RF MEMS varactors, IEEE Trans. Appl. Supercond. **24**, 150709 (2014).

[11] S. H. Talisa, M. A. Janocko, C. Moskowitz, J. Talvacchio, J. F. Billing, R. Brown, D. C. Buck, K. Jones, B. R. McAvoy, G. R. Wagner, and D. H. Watt, Low- and

high-temperature superconducting microwave filters, IEEE Trans. Microw. Theory Tech. **39**, 1448 (1991).

[12] M. Tanaka, H. Akaike, A. Fujimaki, Y. Yamanashi, N. Yoshikawa, S. Nagasawa, K. Takagi, and N. Takagi, 100-GHz single-flux-quantum bit-serial adder based on 10-kA/cm^2 niobium process, IEEE Trans. Appl. Supercond. **21**, 792 (2011).

[13] M. Reagor, W. Pfaff, C. Axline, R. W. Heeres, N. Ofek, K. Sliwa, E. Holland, C. Wang, J. Blumoff, K. Chou, M. J. Hatridge, L. Frunzio, M. H. Devoret, L. Jiang, and R. J. Schoelkopf, Quantum memory with millisecond coherence in circuit QED, Phys. Rev. B **94**, 014506 (2016).

[14] A. A. Murthy, P. M. Das, S. M. Ribet, C. Kopas, J. Lee, M. J. Reagor, L. Zhou, M. J. Kramer, M. C. Hersam, M. Checchin, A. Grassellino, R. dos Reis, V. P. Dravid, and A. Romanenko, Developing a chemical and structural understanding of the surface oxide in a niobium superconducting qubit, ACS Nano **16**, 17257 (2022).

[15] G. A. Hernandez, R. Bai, Y. Cao, J. A. Sellers, C. D. Ellis, D. B. Tuckerman, and M. C. Hamilton, Microwave performance of niobium/kapton superconducting flexible cables, IEEE Trans. Appl. Supercond. **27**, 1200104 (2017).

[16] V. Gupta, B. Yelamanchili, S. Zou, T. Isaacs-Smith, J. A. Sellers, D. B. Tuckerman, and M. C. Hamilton, Thin-film Nb/polyimide superconducting stripline flexible cables, IEEE Trans Appl. Supercond. **29**, 1501605 (2019).

[17] P. V. Tyagi, M. Doleans, B. Hannah, R. Afanador, C. McMahan, S. Stewart, J. Mammosser, M. Howell, J. Saunders, B. Degraff, and S. H. Kim, Improving the work function of the niobium surface of SRF cavities by plasma processing, Appl. Surf. Sci. **369**, 29 (2016).

[18] W. Keijers, X. D. Baumans, R. Panghotra, J. Lombardo, V. S. Zharinov, R. B. Kramer, A. V. Silhanek, and J. Van de Vondel, Nano-SQUIDs with controllable weak links created: Via current-induced atom migration, Nanoscale **10**, 21475 (2018).

[19] J. Lombardo, Željko L. Jelić, X. D. Baumans, J. E. Scheerder, J. P. Nacenta, V. V. Moshchalkov, J. Van de Vondel, R. B. Kramer, M. V. Milošević, and A. V. Silhanek, In situ tailoring of superconducting junctions via electro-annealing, Nanoscale **10**, 1987 (2018).

[20] S. Collienne, B. Raes, W. Keijers, J. Linek, D. Koelle, R. Kleiner, R. B. Kramer, J. Van de Vondel, and A. V. Silhanek, Nb-Based Nanoscale Superconducting Quantum Interference Devices Tuned by Electroannealing, Phys. Rev. Appl. **15**, 034016 (2021).

[21] S. Collienne, D. Majidi, J. Van de Vondel, C. B. Winkelmann, and A. V. Silhanek, Targeted modifications of monolithic multiterminal superconducting weak-links, Nanoscale **14**, 5425 (2022).

[22] S. B. Alvarez, J. Brisbois, S. Melinte, R. B. Kramer, and A. V. Silhanek, Statistics of thermomagnetic breakdown in Nb superconducting films, Sci. Rep. **9**, 3659 (2019).

[23] J. Evertsson, F. Bertram, F. Zhang, L. Rullik, L. R. Merte, M. Shipilin, M. Soldemo, S. Ahmadi, N. Vinogradov, F. Carlà, J. Weissenrieder, M. Göthelid, J. Pan, A. Mikkelsen, J.-O. Nilsson, and E. Lundgren, The thickness of native oxides on aluminum alloys and single crystals, Appl. Surf. Sci. **349**, 826 (2015).

[24] J. M. Rowell, M. Gurvitch, and J. Geerk, Modification of tunneling barriers on Nb by a few monolayers of Al, Phys. Rev. B **24**, 2278 (1981).

[25] M. Nonnenmacher, M. P. O'Boyle, and H. K. Wickramasinghe, Kelvin probe force microscopy, Appl. Phys. Lett. **58**, 2921 (1991).

[26] W. Melitz, J. Shen, A. C. Kummel, and S. Lee, Kelvin probe force microscopy and its application, Surf. Sci. Rep. **66**, 1 (2011).

[27] Z. M. Wu, M. Steinacher, R. Huber, M. Calame, S. J. V. D. Molen, and C. Schönenberger, Feedback controlled electromigration in four-terminal nanojunctions, Appl. Phys. Lett. **91**, 053118 (2007).

[28] T. Aref and A. Bezryadin, Precise in situ tuning of the critical current of a superconducting nanowire using high bias voltage pulses, Nanotechnology **22**, 395302 (2011).

[29] X. D. A. Baumans, A. Fernandez-Rodriguez, N. Mestres, S. Collienne, J. V. de Vondel, A. Palau, and A. V. Silhanek, Electromigration in the dissipative state of high-temperature superconducting bridges, Appl. Phys. Lett. **114**, 012601 (2019).

[30] J. Lombardo, S. Collienne, A. Petrillo, E. Fourneau, N. D. Nguyen, and A. V. Silhanek, Electromigration-induced resistance switching in indented Al microstrips, New J. Phys. **21**, 113015 (2019).

[31] F. B. Hagedorn and P. M. Hall, Right-angle bends in thin strip conductors, J. Appl. Phys. **34**, 128 (1963).

[32] K. Kanaya and S. Okayama, Penetration and energy-loss theory of electrons in solid targets, J. Phys. D: Appl. Phys **5**, 43 (1972).

[33] J. Li, B. Hoekstra, Z.-B. Wang, J. Qiu, and Y.-K. Pu, Secondary electron emission influenced by oxidation on the aluminum surface: The roles of the chemisorbed oxygen and the oxide layer, Plasma Sources Sci. Technol. **27**, 044002 (2018).

[34] T. T. Magkoev and G. G. Vladimirov, Aluminium oxide ultrathin-film growth on the Mo(110) surface: A work-function study, J. Phys.: Condens. Matter **13**, L655 (2001).

[35] M. Grundner and J. Halbritter, XPS and AES studies on oxide growth and oxide coatings on niobium, J. Appl. Phys. **51**, 397 (1980).

[36] S. Halas and T. Durakiewicz, Is work function a surface or a bulk property?, Vacuum **85**, 486 (2010).

[37] Q. G. Wang and J. X. Shang, First-principles study on the incipient oxidization of Nb(110), J. Phys.: Condens. Matter **24**, 225005 (2012).

[38] F. Lacy, Developing a theoretical relationship between electrical resistivity, temperature, and film thickness for conductors, Nanoscale Res. Lett. **6**, 636 (2011).

[39] R. K. Williams, V. H. Butler, R. S. Graves, and J. P. Moore, Experimental and theoretical evaluation of the phonon thermal conductivity of niobium at intermediate temperatures, Phys. Rev. B **28**, 6316 (1983).

[40] R. G. Morris and J. G. Hust, Thermal conductivity measurements of silicon from 30° to 425°C, Phys. Rev. **124**, 1426 (1961).

[41] E. T. Swartz and R. O. Pohl, Thermal boundary resistance, Rev. Mod. Phys. **61**, 605 (1989).

[42] A. Giri and P. E. Hopkins, A review of experimental and computational advances in thermal boundary conductance and nanoscale thermal transport across solid interfaces, Adv. Funct. Mater. **30**, 201903857 (2020).

[43] L. P. H. Jeuregns, W. G. Sloof, F. D. Tichelaar, and E. J. Mittemeijer, Growth kinetics and mechanisms of aluminum-oxide films formed by thermal oxidation of aluminum, J. Appl. Phys. **92**, 1649 (2002).

[44] J. Kwo, G. K. Wertheim, M. Gurvitch, and D. N. Buchanan, X-ray photoemission spectroscopy study of surface oxidation of Nb/Al overlayer structures, Appl. Phys. Lett. **40**, 675 (1982).

[45] J. Halbritter, On the oxidation and on the superconductivity of niobium, Appl. Phys. A **43**, 1 (1987).

[46] E. Trabaldo, A. Kalaboukhov, R. Arpaia, E. Wahlberg, F. Lombardi, and T. Bauch, Mapping the Phase Diagram of a $YBa_2Cu_3O_{7-\delta}$ Nanowire through Electromigration, Phys. Rev. Appl. **17**, 024021 (2022).

[47] J. Canet-Ferrer, E. Coronado, A. Forment-Aliaga, and E. Pinilla-Cienfuegos, Correction of the tip convolution effects in the imaging of nanostructures studied through scanning force microscopy, Nanotechnology **25**, 395703 (2014).

[48] K. Ohnishi, T. Kimura, and Y. Otani, Improvement of superconductive properties of mesoscopic Nb wires by Ti passivation layers, Appl. Phys. Express **1**, 021701 (2008).